CLINICAL CANCER RESEARCH | NOVEL BIOMARKERS AND PRECISION MEDICINE

Nonmetastatic Para-aortic Lymph Node Remodeling as a Predictor of Outcome in Locally Advanced Cervical Cancer

Louis Baudin[1], Léa Zanella[1], Alizée Lebeau[2,3], Clémence Pleyers[4], Noémie Gubbels[1], Silvia Blacher[1], Laurence Seidel[5], Athanasios Kakkos[2], Frédéric Goffin[2], Pierre Lovinfosse[6], Christine Gennigens[3], Sébastien Pirson[1], Frédéric Kridelka[2], and Agnès Noel[1]

ABSTRACT

Purpose: Treatment of locally advanced cervical cancer (LACC) is guided notably by the European Society of Gynaecological Oncology guidelines; unfortunately, relapse remains frequent despite standard chemoradiotherapy and brachytherapy. We evaluated whether histologic assessment of nonmetastatic para-aortic lymph nodes (PAoLN) provides prognostic value in LACC.

Experimental Design: Primary tumor and PAoLNs from 137 patients with nonmetastatic LACC were stratified by pretherapeutic ^{18}F-2′-deoxy-2′-fluorodeoxyglucose PET/CT into pelvic PET–positive (pPET^{+}, $n = 72$) and pelvic PET–negative (pPET^{-}, $n = 65$) groups. Immunohistochemistry on whole sections assessed germinal centers, CD4^{+}, CD8^{+}, FOXP3^{+} cells, neutrophils [CD66b^{+}, neutrophil extracellular traps (NET)], and high-endothelial venules (HEV). Associations with progression-free survival (PFS) were examined via uni- and multivariate analyses after a median follow-up of 55.4 months.

Results: The primary tumor profile was not associated with outcome, whereas PAoLN features were strongly predictive. In pPET^{-} patients, higher NETs were associated with shorter PFS [$P = 0.015$; hazard ratio (HR) = 2.768], whereas an elevated CD4/CD8 ratio improved outcomes ($P = 0.047$, HR = 0.497). In pPET^{+} patients, shorter PFS was linked to FOXP3^{+} ($P = 0.04$, HR = 1.918) and proliferating FOXP3^{+} cell ($P = 0.018$, HR = 1.668) density. Across the full cohort, abundant germinal centers ($P = 0.0355$, HR = 0.273) and an elevated CD4/CD8 ratio ($P = 0.001$, HR = 0.490) independently correlated with lower recurrence risk. Internal validation was conducted through a bootstrap resampling method. Combinatorial analyses revealed distinct predictive signatures according to pPET status: higher NETs, fewer germinal centers, and International Federation of Gynaecology and Obstetrics IIA1 to IIIB status predicted relapse in pPET^{-} patients.

Conclusions: Integrating pPET status with PAoLN histologic analyses improves recurrence risk stratification in LACC. PAoLN evaluation may serve as a complementary tool to guide treatment intensification and surveillance strategies.

Introduction

Cervical cancer accounts for approximately 660,000 new cases and 350,000 deaths annually, ranking as the fourth most common malignancy and cause of cancer-related mortality among women worldwide (1). Notably, it is the second leading cause of cancer death among women aged 18 to 44 years across both high-income and low- to middle-income countries (GLOBOCAN 2022). The clinical management and prognosis of cervical cancer are guided by the disease stage as defined by the International Federation of Gynaecology and Obstetrics (FIGO) classification system (2). The disease progresses from early stage, defined by tumors <4 cm confined to the cervix, to locally advanced cervical carcinoma (LACC), characterized by tumors >4 cm and/or extension into adjacent pelvic structures. In 2018, the FIGO staging system was revised to incorporate imaging and pathologic findings, including the lymph node (LN) status [not metastatic (M0)/metastatic (M^{+})] due to their prognostic significance. The detection of LN metastases by imaging modalities automatically upstages FIGO stage IIIC1 for pelvic LNs to stage IIIC2 for para-aortic (PAo) LNs (PAoLN), irrespective of primary tumor size or local spread. Indeed, LN involvement is a strong prognostic factor, associated with a higher recurrence risk and poorer overall survival (OS; refs. 3–6). According to European Society of Gynaecological Oncology/European Society for Radiotherapy and Oncology/European Society of Pathology guidelines, the standard treatment for LACC (FIGO 2018 stages IB3–IVA) consists of cisplatin-based concurrent chemoradiotherapy followed by brachytherapy. Treatment is further tailored according to the nodal status assessed either by pretherapeutic PET/CT using ^{18}F-2′-deoxy-2′-fluorodeoxyglucose imaging (referred to below as PET) or by LN surgical staging. In cases of nodal involvement, management may include an external beam radiotherapy boost to the affected LN and an extended field of radiotherapy to the PAo area (7). In the current era of treatment de-escalation and precision surgery, the role of PAo lymphadenectomy is increasingly being questioned,

---

[1] Laboratory of Tumor and Development Biology, GIGA, University of Liège (ULiège), Liège, Belgium. [2] Department of Obstetrics and Gynecology, University Hospital of Liege (CHU-Liège), Liège, Belgium. [3] Department of Medical Oncology, University Hospital of Liège (CHU-Liège), Liège, Belgium. [4] Department of Oncological Radiotherapy, University Hospital of Namur (CHU-UCL-Namur), Namur, Belgium. [5] Biostatistics and Research Method Center (B-STAT), CHU-ULiège, Liège, Belgium. [6] Department of Nuclear Medicine and Oncological Imaging, University Hospital of Liège (CHU-Liège), Liège, Belgium.

L. Baudin and L. Zanella contributed equally to the article.

A. Noel and F. Kridelka are co-senior authors.

Corresponding Author: Agnès Noel, Laboratory of Tumor and Development Biology, Tour de Pathologie, B23, +4; Avenue Hippocrate, 13, Liège 4000, Belgium. E-mail: agnes.noel@uliege.be

Clin Cancer Res 2026;XX:XX–XX

doi: 10.1158/1078-0432.CCR-25-3894

Translational Relevance

Despite multimodal therapy, patients with locally advanced cervical cancer (LACC) face a high risk of relapse, and current International Federation of Gynaecology and Obstetrics (FIGO) 2018 staging provides limited prognostic discrimination. Our study demonstrates that histologic evaluation of para-aortic lymph nodes (PAoLN), when integrated with pelvic ^{18}F-2′-deoxy-2′-fluorodeoxyglucose PET/CT status, refines recurrence risk assessment beyond conventional staging. Distinct immune signatures in PAoLNs—particularly germinal center activity, FOXP3$^+$ T-cell expansion, CD4/CD8 ratio, and neutrophil extracellular trap (NET) density—identified subgroups of patients with differential relapse risk. The global multivariate model was translated into a nomogram incorporating three factors to facilitate individualized risk assessment in clinical practice. These findings highlight the clinical value of PAoLN immune profiling as a complementary biomarker strategy, which may enable more precise stratification of patients for treatment intensification or tailored surveillance.

particularly in patients with negative PET findings. Indeed, this surgical procedure is associated with increased complications and morbidity, and its diagnostic and therapeutic benefit remains unclear (8–11). Despite advances in multimodal treatment, including surgical staging, about one third of patients with LACC treated with concurrent chemoradiotherapy and brachytherapy experience recurrence (12, 13).

The persistent risk of relapse highlights the need to identify reliable risk signatures at diagnosis, ideally within primary tumors and/or within PAoLNs, to improve recurrence risk stratification in patients with LACC and individualize their treatment. In this study, we investigated immunologic modulation within the primary tumor and PAoLN at the time of diagnosis, focusing on key immune variables including B-cell germinal centers; CD4$^+$, CD8$^+$, and FOXP3$^+$ T cells; neutrophils; neutrophil extracellular traps (NET); and high-endothelial venules (HEV) as critical regulators of lymphocyte trafficking and immune surveillance. We evaluated whether immunologic alterations varied within PAoLN of patients with positive versus negative pelvic PET (pPET) findings and correlated with clinical outcomes. Primary tumors were also analyzed to assess corresponding histopathologic features. We provide evidence that pPET scan status, when integrated with PAoLN analyses, but not primary tumor features, is a reliable predictor of recurrence risk. Our study highlights the added value of PAoLN staging to identify patients with LACC most likely to benefit from treatment intensification and/or more cautious follow-up.

Materials and Methods

Human tissue samples

The retrospective single-center cohort included 155 female patients diagnosed with LACC and treated at the University Hospital of Liège (Belgium) between May 2010 and April 2022. The median age was 52 years. LACC stage was defined according to the FIGO 2018 classification (IB3–IVA). To be eligible, patients must (i) have received a diagnostic/pretreatment PET scan, (ii) have undergone laparoscopic PAo lymphadenectomy, (iii) have been treated with concomitant chemoradiotherapy (CCRT) followed by brachytherapy, and (iv) have no detectable metastasis in PAoLNs through histologic examination. The overall prevalence of human papillomavirus (HPV) positivity was 98%. Given this minimal variability in HPV status, particularly within the squamous cell carcinoma (SCC) subgroup, in which all tumors were HPV$^+$, HPV infection was not included as an independent covariate in the multivariable models, as its near-uniform distribution precluded meaningful stratified or adjusted analyses (Supplementary Table S1).

Formalin-fixed, paraffin-embedded LNs and/or primary tumor samples collected before treatment were available for all patients and provided by the Biobank of the University Hospital of Liège (Belgium). All specimens were reviewed by experienced pathologists and classified as metastatic or nonmetastatic. Clinical and pathologic data were retrieved from electronic medical records. Patients with incomplete clinical data or unavailable tissue material were excluded.

The study protocol was approved by the Institutional Ethics Committee of the University Hospital of Liège (2024-438). The use of human body material from the biobank does not require consent forms (Belgian law of December 19, 2008).

Immunofluorescence on human LN sections

PAoLN and primary tumor biopsies from patients with LACC were fixed in 4% formaldehyde directly after lymphadenectomy or tumor biopsy, respectively. Then, they were paraffin-embedded and sectioned at 4 μm. Tissue sections were rehydrated through successive xylene, alcohol, and water baths. Heat-induced antigen retrieval was performed using Dako target retrieval buffer at pH 9.0 (Dako, S2367). After cooling for 20 minutes and rinsing with water, nonspecific background noise was reduced using TrueBlack (Cell Signaling Technology, 92401 S). Slides were then blocked with an animal-free blocking solution (Cell Signaling Technology, 15019 L) for 30 minutes, followed by incubation with the primary antibody of interest diluted in antibody diluent (Dako, S2022) for 1 hour at room temperature or overnight at 4°C in a humidified darkroom. Samples were washed with PBS and incubated with the appropriate secondary antibody. These steps were repeated for combined stainings. Slides were mounted with DAPI mounting media (SouthernBiotech, 0100-20).

Different combinations of antibodies were applied to serial sections of primary tumors and PAoLNs. Primary tumor sections were labeled with combinations of CD4/CD8/alpha smooth muscle actin (αSMA)/cytokeratin, CD66b/FOXP3/cytokeratin/αSMA, and PNAd/cytokeratin/αSMA. For PAoLNs, stainings included PNAd, CD4/CD8, CD66b/FOXP3/Ki67, and citrullinated histone H3 (H3cit)/myeloperoxidase (MPO).

The antibodies and all associated information are listed in Supplementary Table S2.

Virtual image acquisition and quantification

Virtual images were acquired with SLIDEVIEW VS200 from Olympus at 20× magnification (Olympus), equipped with a UPlanXApo 20× 0.8 objective (Olympus) and a Hamamatsu ORCA-Flash camera, using DAPI, FITC, Cy3, Cy5, and Cy7 filter sets. All quantitative analyses were conducted on whole tissue sections using QuPath software version 0.5.1 (RRID: SCR_018257) to determine either the stained area or the number of positive cells/structures (HEV, germinal center). For CD4$^+$ and CD8$^+$ cell evaluation, density was defined as the ratio of the stained area to the stromal section area. For FOXP3$^+$ cells, CD66b$^+$ cells, NETs, germinal centers, and HEVs, density represents cell/structure number/mm^2.

With respect to primary tumor samples, stromal versus tumor segmentation was computationally performed based on cytokeratin positivity. Tumor-associated HEVs (TA-HEV) were defined as an object displaying a lumen and covered by αSMA-positive (αSMA$^+$) cells, with PNAd detection on the lumen side.

For PAoLN samples, the total number of HEVs was automatically counted by detecting every PNAd$^+$ structure larger than 100 μm^2 to omit putative artefactual objects. Lumenized HEVs were hand-detected, and their lumens were measured manually. To decrease slice sectioning bias, the smallest diameter was considered for complex vessels. Dilated HEVs are defined as HEVs displaying a lumen larger than 20 μm. A total of 36,841 HEVs and 2,475 dilated HEVs were analyzed for the pPET$^-$ group, and 52,748 HEVs and 2,204 dilated HEVs were analyzed for the pPET$^+$ patient group. Results were expressed as a percentage of dilated HEVs. NETs were quantified based on the colocalization of MPO and H3Cit staining.

Statistical methods

All the data were tested for normality by the Shapiro–Wilk test. Some parameters were log-transformed or square root transformed before their use in statistical models. Comparisons between groups were done with the Kruskal–Wallis H test followed by Dunn's multiple comparison or the Mann–Whitney U test, as specified in the figure legends. Data are shown using the median with IQRs. Statistical significance was determined at $P < 0.05$, denoted as follows: *, $P < 0.05$; **, $P < 0.01$; ***, $P < 0.001$; ****, $P < 0.0001$.

The association between continuous variables was assessed using Spearman's rank correlation coefficient (r_s). To identify the most predictive signatures of relapse derived from multiple parameters, we applied an unbiased, combinatorial Cox regression–based predictive model approach. First, each parameter was evaluated individually (univariate analysis). Next, all possible pairwise (2 × 2) and triplet (3 × 3) combinations were assessed. To prevent the generation of subgroups too small for meaningful statistical interpretation, we applied a minimum threshold of six patients per group (approximately 10% of both the pPET$^-$ and pPET$^+$ populations). For each tested combination, two subgroups were generated: (i) patients meeting all combined criteria and (ii) all remaining patients. For every subgroup, we recorded the total number of patients, the number of relapse events, and the corresponding P value. Table A (Supplementary Figures S1 and S2) reports the data for each variable analyzed independently, whereas Tables B and C present only the data for those parameter combinations that significantly predicted relapse of the respective subgroups. All the used cutoff values are indicated in the figures, which correspond to the median of each patient group (pPET$^-$ and pPET$^+$) when considering continuous variables.

Progression-free survival (PFS) was analyzed according to the studied continuous variables (group-related) using Cox proportional hazards (PH) regression. The Schoenfeld residuals test was performed for each model to assess the PH assumption. In cases where the PH assumption was not met (indicated by † in the tables), the model was corrected by adding an interaction term between the parameter and time (the interval between staging and relapse/last follow-up). Variables with a P value <0.10 in univariate analysis were then included in the multivariate model. When the PH assumption was not met in univariate analysis, both the variable and the variable × time interaction were entered into the model if the variable remained significant after correction. Multivariate Cox regression with stepwise selection was subsequently applied to the selected variables. In some instances, Firth's correction was used. For uni- and multivariate analyses, the P value, the hazard ratio (HR) with its 95% confidence interval (CI), the results of the PH test, and the adjusted P values were reported for each variable. Multivariate analyses display only the statistically significant variables ($P < 0.05$). Statistical significance was set at a two-sided 5% level ($P < 0.05$). The dataset was bootstrapped 500 times to check the stability of the multivariate models. The model was applied to each resampling, and Harrel's C-index was derived. The mean and SD of the 500 obtained C-indexes were calculated to give an estimation of the mean and the precision (SE) of the original model. Multivariate Cox PH models were constructed by integrating clinical parameters, PET imaging status, and PAoLN immune/vascular features identified as significant in univariate analyses. Area under the curve (AUC) over time was graphically reported to assess prognostic performance throughout follow-up. A nomogram was generated from the final multivariable models to provide individualized estimates of PFS at 12, 24, and 36 months. Cumulative incidence functions (CIF) were estimated within a competing risks framework. Locoregional recurrences (LRR) and distant recurrences (DR) were considered distinct failure types, whereas patients without recurrence were treated as censored. CIFs were computed using the Fine and Gray subdistribution hazard approach, providing direct estimates of the probability of each recurrence type over time. These time-dependent incidence estimates were subsequently combined with recurrence site information to construct time-resolved failure maps, allowing spatial visualization of recurrence patterns across follow-up.

Statistical analyses were performed using GraphPad Prism 9.0 (GraphPad Software, RRID: SCR_002798), SAS version 9.4 (RRID: SCR_008567), and R version 4.5.1 (RRID: SCR-001905).

Results

Workflow of the study

In cervical cancer, most metastases typically progress stepwise, spreading from the pelvic region (primary tumor and pelvic LNs) to the PAoLNs. The patient cohort and sample overview are schematically illustrated in **Fig. 1**, with PAoLN metastasis assessed histologically (PAoLN$^+$ vs. PAoLN$^-$; **Fig. 1A**) and PET scan used to classify patients as negative (pPET$^-$) or positive (pPET$^+$) for pelvic nodes (**Fig. 1B**). Primary tumor and PAoLN samples were subsequently analyzed via immunohistochemistry (IHC; **Fig. 1C**) for key immune and stromal markers to identify microenvironmental signatures associated with recurrence risk. To ensure an unbiased approach and consider tissue heterogeneity, stained samples were whole-scanned and subjected to semiautomatic computerized quantification (**Fig. 1C**).

Between 2010 and 2022, 155 patients with LACC were treated at the University Hospital of Liège (**Fig. 1D**). Eighteen patients with PAoLN metastases at diagnosis were excluded, resulting in 137 eligible patients. The cohort was divided into two subgroups: 72 patients classified as pPET$^-$ (no pelvic node uptake) and 65 as pPET$^+$ (pelvic node uptake). Biomarker analyses were performed in all 137 patients using pretreatment samples obtained at diagnosis. For survival analyses, seven patients who received additional treatments were excluded to obtain a final cohort of 130 patients uniformly treated with CCRT followed by image-guided brachytherapy (IGBT).

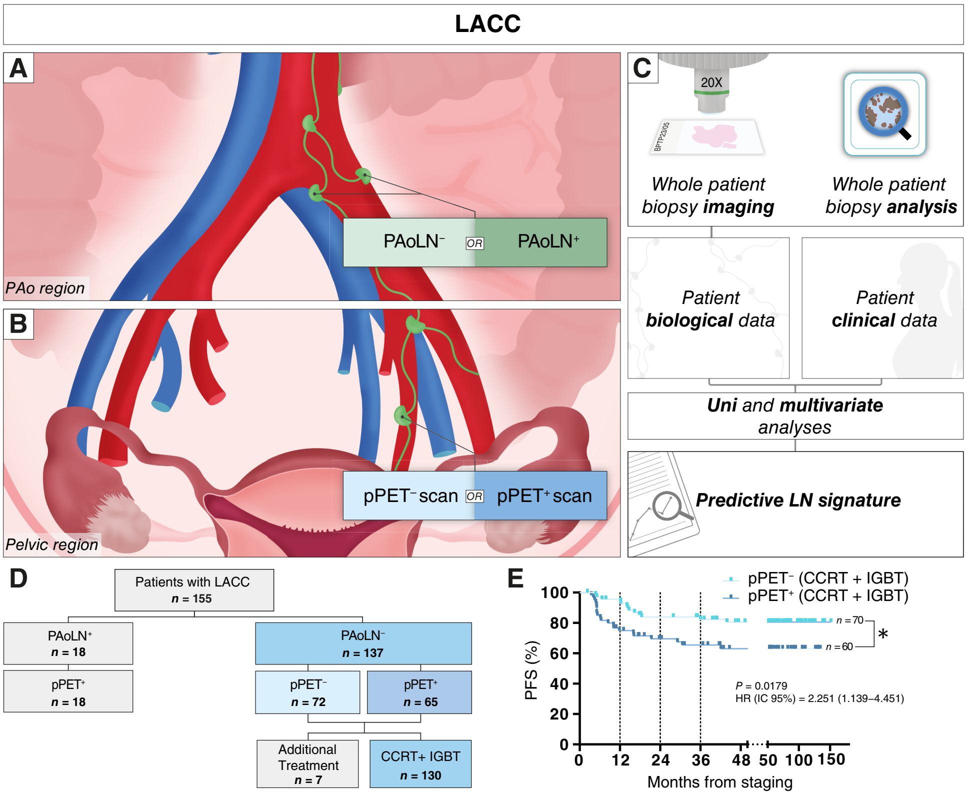

Figure 1.

Study design and clinicopathologic features of patients with LACC. **A** and **B,** Schematic representation of the para-aortic (**A**) and pelvic (**B**) regions in patients with cervical cancer. The retrospective cohort includes primary tumor and PAo (PAoLN) samples from patients with LACC ($n = 155$), stratified by the absence (PAoLN$^-$) or presence (PAoLN$^+$) of metastatic PAoLNs assessed through histologic examination. Pelvic disease status was defined by PET as negative (pPET$^-$) or positive (pPET$^+$) (**B**). **C,** Workflow of immunohistochemical analyses of patient biopsies. Whole tissue sections were imaged and computationally analyzed using QuPath software. Uni- and multivariate statistical analyses were performed to identify predictive signatures integrating biological parameters with clinical data. **D,** The cohort included 155 patients: 18 patients had metastatic PAoLN, and 137 did not (regardless of pPET scan status). Uni- and multivariate analyses were performed in the subgroup of 130 patients who received uniform treatment with CCRT followed by IGBT. **E,** Kaplan–Meier plots showing the impact of pPET status on PFS in patients treated with CCRT and IGBT. Log-rank test; *, $P < 0.05$.

The clinical and pathologic characteristics of the patients are summarized in Supplementary Table S3. The median age was 52 years. All patients underwent PAoLN staging, allowing confirmation of PAoLN negative (PAoLN$^-$) status. SCC was the predominant histologic subtype (84.7%). FIGO stages IIIC1 to IVA represented 50% of cases, followed by IIA1 to IIIB (35.8%) and IB3 (13.1%). The median tumor size on MRI was 48 mm (IQR: 39–56 mm). The median interval time from staging to treatment completion was 2.4 months. On PET scan, pelvic LNs were considered positive and negative in 52.5% and 47.4%, respectively. pPET scan positivity in patients treated with combined CCRT and IGBT conferred a two-fold higher risk of recurrence [HR (95% CI), 2.251 (1.139–4.451); **Fig. 1E**], underscoring its association with adverse prognosis in patients with LACC. Given that pPET scan status was predictive of recurrence and patient characteristics were well balanced (Supplementary Table S3), all analyses were stratified according to pPET$^+$ and pPET$^-$ groups.

The median follow-up was 55.4 months. The 5-year OS and PFS were 73.83% and 72.53%, respectively. During follow-up, recurrence was observed in 34 patients (26.2%), and 28 patients (21.5%) died from cancer.

T-cell infiltration profile differs in primary tumors of patients according to pPET status

IHC was conducted on the available primary tumor samples obtained from patients with nonmetastatic PAoLN disease (PAoLN$^-$; $n = 91$). Immune markers were quantified within the stromal compartment delineated through cytokeratin staining (**Fig. 2A–C**). The CD4/CD8 ratio was significantly reduced in patients with a positive pPET scan (**Fig. 2D**). This may be explained by CD8 density, which tended to increase in these patients, whereas CD4 density was similar in pPET$^+$ and pPET$^-$ patients (**Fig. 2E** and **F**). Densities of FOXP3$^+$ cells and CD66b$^+$ cells were indistinguishable between the two patient groups (**Fig. 2G** and **H**). These results reflect a differential profile of CD8 T-cell infiltration in the tumor stroma of patients according to pPET status.

The pattern of TA-HEVs differs according to pPET status

Given their established role in immune cell recruitment, we also quantified the density of TA-HEVs, defined as lumenized peripheral node addressin positive vascular structures (PNAd$^+$ vessels) covered by αSMA$^+$ cells, within the tumor stroma (**Fig. 2I**). Based on the median and quartile distribution of TA-HEV density, samples were classified into four categories: class I (0 vessels/mm^2), class II

(0–1.173 vessels/mm^2), class III (1.173–4.362 vessels/mm^2), and class IV (4.362–22.644 vessels/mm^2; **Fig. 2J**). Overall, PNAd$^+$ vessel density tended to decrease in the pPET$^+$ group compared with the pPET$^-$ group although this difference did not reach statistical significance (**Fig. 2K**). When stratifying by TA-HEV class, tumors from pPET$^+$ patients display a shift toward lower TA-HEV classes, with an enrichment in classes I and II (58%) and a relative reduction in classes III and IV (32%; **Fig. 2L**). In contrast, tumors of pPET$^-$ patients showed the opposite distribution (43.5% of classes I + II and 56.5% of classes III + IV).

We next examined the relationship between TA-HEV classes and immune cell infiltration (**Fig. 2M–P**). In pPET$^-$ patients, higher TA-HEV classes were associated with increased densities of both CD8 and CD4 ($P < 0.05$; **Fig. 2M** and **N**). In contrast, in pPET$^+$ patients, T-cell densities remained stable across all vessel classes. CD66b$^+$ or FOXP3$^+$ cell infiltration did not vary significantly across TA-HEV classes or between patient groups (**Fig. 2O** and **P**). Nonetheless, TA-HEV density showed a weak but significant positive correlation with CD4$^+$ cell density (Spearman's $r_s = 0.2467$, $P = 0.0191$), whereas no such correlation was found with CD66b, FOXP3, or CD8 cell densities. Collectively, these findings indicate that TA-HEVs exhibit distinct patterns in the tumor stroma of pPET$^+$ vs pPET$^-$ patients, but their relationship with immune cell infiltration remains limited.

Primary tumor profiles are not associated with relapse risk in univariate analyses

PFS was evaluated using Cox regression for each parameter assessed on the primary tumor. All biological variables and clinical characteristics were included in the analysis (Supplementary Table S4). Univariate analyses of the primary tumor did not identify any variables as prognostic indicators of relapse when patients were stratified according to pPET status (Supplementary Table S4). Univariate followed by multivariate analyses were performed on all available primary tumor samples uniformly treated with CCRT + IGBT ($n = 87$). The multivariate analysis revealed that tumor size was negatively correlated with PFS [$P = 0.0147$; HR (95% CI), 1.071 (1.014–1.132)], whereas elevated FOXP3$^+$ cell density was protective [$P = 0.0267$; HR (95% CI), 0.623 (0.410–0.947)]. Therefore, we decided to apply a similar methodology to PAoLNs$^-$ to assess their impact. The clinical and pathologic characteristics of the patients for these analyses are summarized in Supplementary Table S5.

PAoLNs of pPET$^+$ patients display a more dynamic immune response

We next focused our study on nonmetastatic PAoLNs of pPET$^+$ and pPET$^-$ patients with LACC ($n = 129$; Supplementary Fig. S1). The number of germinal centers was higher in pPET$^+$ patients compared with pPET$^-$ patients, suggesting a more dynamic immune response in the former group (**Fig. 3A**). The density of CD4$^+$ cells was comparable between the two patient groups. However, the CD4/CD8 ratio tended to be lower in PET$^+$ samples, likely driven by a modest, though not statistically significant, increase in CD8$^+$ cell density ($P > 0.05$, **Fig. 3B–D**). In contrast, FOXP3$^+$ cells and proliferating FOXP3$^+$Ki67$^+$ cells were significantly enriched in pPET$^+$ patients ($P < 0.01$ and $P < 0.05$, respectively; **Fig. 3E** and **F**). To accurately assess neutrophil involvement (infiltration and activity), we immunostained CD66b$^+$ cells and detected NETs through both H3Cit and MPO staining on serial sections (**Fig. 3G** and **H**). CD66b$^+$ cell density was significantly enhanced in pPET$^+$ patients ($P < 0.05$), accompanied by a trend toward increased NET formation (**Fig. 3G** and **H**).

Finally, we evaluated HEVs, specialized vascular structures within LNs that facilitate lymphocyte trafficking. Under inflammatory or tumoral conditions, HEVs can become dilated (lumen >20μm), a change thought to impair immune cell recruitment (14). The proportion of dilated HEVs did not differ significantly between the two patient groups ($P = 0.055$; **Fig. 3I**). Notably, the frequency of dilated HEVs correlated negatively with CD8$^+$ cell density (Spearman's $r_s = 0.2319$, $P = 0.0098$) but showed no significant association with CD4$^+$, CD66b$^+$, or FOXP3$^+$ cell densities ($P > 0.05$, **Fig. 3J–M**). In conclusion, nonmetastatic PAoLNs of pPET$^+$ patients display features of increased immune activity—including increased germinal center formation, FOXP3$^+$ cell expansion, and neutrophil infiltration—while preserving HEV architecture that likely supports sustained lymphocyte recruitment.

Multi- and univariate analyses in the PAoLN

PFS was evaluated in relation to clinical parameters (pPET, histology, FIGO stage, age, tumor size) and PAoLN biological features (neutrophils, NETs, FOXP3$^+$ cells, FOXP3$^+$Ki67$^+$ cells, germinal centers, CD4/CD8 ratio, dilated HEVs). The corresponding clinical and pathologic characteristics of patients are summarized in Supplementary Table S5. For pPET$^-$ patients, univariate analyses identified NETs [$P = 0.015$; HR (95% CI), 2.768 (1.215–6.304)] and CD4/CD8 ratio [$P = 0.047$; HR (95% CI), 0.497 (0.250–0.989)] as prognostic markers (**Table 1**). In contrast, the relapse risk of pPET$^+$ patients was found to be significantly associated with FOXP3$^+$ [$P = 0.04$; HR (95% CI), 1.918 (1.029–3.575)] and FOXP3$^+$Ki67$^+$ [proliferating FOXP3$^+$ cells; $P = 0.018$; HR (95% CI), 1.668 (1.093–2.544)] cell densities, as well as CD4/CD8 ratio [$P = 0.0097$; HR (95% CI), 0.506 (0.302–0.848); **Table 1**].

We then performed a multivariate analysis on the available samples from the global cohort independently of pPET status ($n = 123$), selecting variables with $P < 0.1$ from the univariate analyses (**Table 1**). pPET positivity emerged as an independent predictive factor [$P = 0.0033$; HR (95% CI), 3.299 (1.488–7.315)], being significantly associated with an increased risk of relapse. Conversely, a high number of germinal centers [$P = 0.0355$; HR (95% CI), 0.273 (0.081–0.915)] and a high CD4/CD8 ratio [$P = 0.001$; HR (95% CI), 0.490 (0.320–0.748)] were independently associated with better PFS. For the pPET$^+$ subgroup, we explored the use of continuous PET parameters, including maximum standardized uptake value, metabolic tumor volume, and total lesion glycolysis. This approach did not improve model performance compared with the binary pPET$^+$ versus pPET$^-$ classification (Supplementary Fig. S6). Internal validation of our model was performed using the bootstrap resampling method with 500 iterations to assess model stability and correct for optimism. The apparent model performance yielded a Harrell's C-index of 0.7434. After bootstrap validation, the optimism-corrected mean (SE) C-index was 0.7536 (0.045), indicating a stable discriminating performance with minimal overfitting.

Integrated predictive model and clinical applicability

Time-dependent AUC analysis (**Fig. 4A**) showed that the model displayed a good and stable discriminative ability over time. After an initial period of instability during the early follow-up, likely related to a limited number of events, the AUC rapidly increased and remained consistently around 0.75 to 0.80 throughout follow-up, indicating a robust capacity to discriminate patients according to

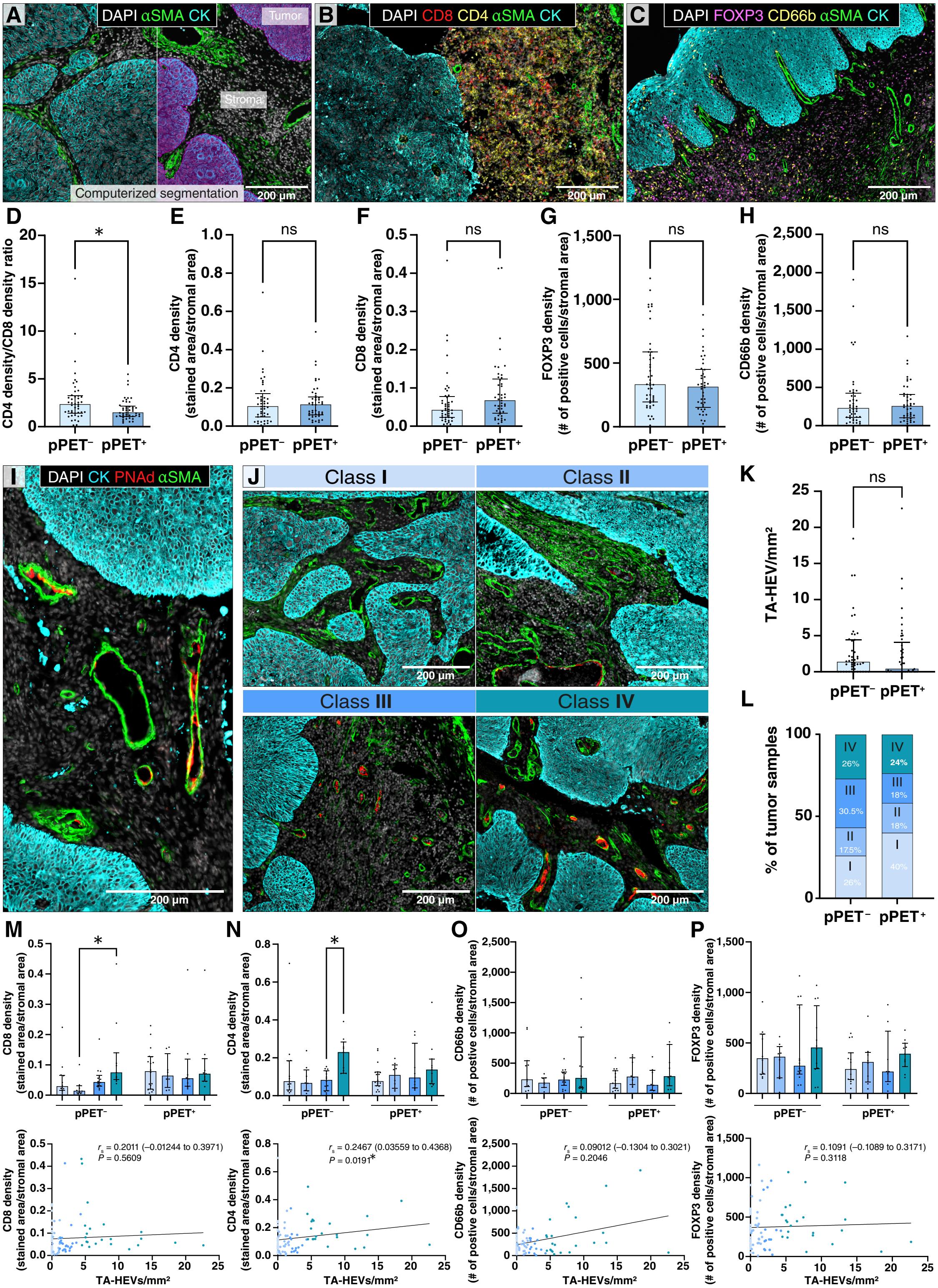

Figure 2.

Immunohistochemical analyses of primary tumors. **A,** Computerized segmentation of the tumor regions. The tumor compartment corresponds to cytokeratin-positive cells (cyan). The stroma is the cytokeratin-negative part containing αSMA-positive structures (green). **B** and **C,** Illustrations of CD4 (yellow) and CD8 (red) T cells (**B**) and CD66b$^+$ (yellow) and FOXP3$^+$ (magenta) cells (**C**). **D–H,** Histograms present the quantifications of

(*Continued on the following page.*)

their risk of recurrence. To integrate clinical, imaging, and PAoLN immune features into a unified prognostic framework, we performed multivariable regression analyses incorporating pPET status, the number of germinal centers, and the CD4/CD8 ratio, which were independently associated with PFS. Based on the final multivariable model, we constructed a nomogram for the global cohort ($n = 123$) to enable individualized prediction of PFS probabilities at 12, 24, and 36 months (**Fig. 4B**).

DR is the predominant type of early therapeutic failure

Recurrences occurring after treatment were categorized as LRR (in local tissues and pelvic LNs) or DR (in PAoLNs and extranodal organs outside the pelvis). Across the whole cohort, DR represents the predominant mode of therapeutic failure over time, with a CIF of 0.10 at 12 months, compared with LRR, which shows a CIF of 0.05 (**Fig. 4C**). Accordingly, 1 year after initial staging and treatment, 10% of patients experienced a distant relapse, and 5% relapsed in the pelvic region, whereas 85% remained recurrence-free. The predominance of DR over LRR was confirmed after dichotomization according to pPET status. Among pPET$^+$ patients, at 12 months, 15% and 10% of patients experienced DR and LRR, respectively. In contrast, among pPET$^-$ patients, despite an overall reduction in the total number of recurrences, the 12-month CIF was 8% for DR and 0% for LRR. Collectively, these time-to-failure patterns suggest that DR occurs more frequently and earlier than LRR, which may reflect effective local disease control and/or more aggressive phenotypes favorable to systemic dissemination.

Distinct prognostic profiles predict relapse risk in pPET$^-$ and pPET$^+$ patients

We conducted a combinatorial Cox regression–based analysis to assess the existence of high-risk patient subgroups within both pPET$^-$ and pPET$^+$ groups. Following median-based univariate analyses, successive evaluations were performed to generate all possible combinations of two or three variables (Supplementary Tables S7 and S8). In pPET$^+$ patients, univariate analysis revealed that a low CD4/CD8 ratio [$P = 0.0092$; HR (95% CI), 3.811 (1.392–10.434)] or high FOXP3$^+$Ki67$^+$ cell density [$P = 0.0369$; HR (95% CI), 2.743 (1.063–7.075)] was significantly associated with increased relapse risk (Supplementary Table S7A). When combining two variables, 10 significant associations emerged, with the most relevant being the CD4/CD8 ratio and germinal centers [$P = 0.0017$; HR (95% CI), 4.038 (1.691–9.640)], the CD4/CD8 ratio and tumor size [$P = 0.0056$; HR (95% CI), 3.402 (1.1431–8.088)], and the CD4/CD8 ratio and FOXP3$^+$ cell density [$P = 0.006$; HR (95% CI), 3.394 (1.420–8.113); Supplementary Table S7B]. Strikingly, the addition of a third variable (CD4/CD8 ratio, FOXP3$^+$ cells, and germinal centers) identified a subgroup of patients with uniformly poorer outcomes, as all patients relapsed [$P = 0.0001$; HR (95% CI), 6.63 (2.613–16.817); **Fig. 5A**; Supplementary Table S7C]. The Kaplan–Meier plot combining these three parameters clearly demonstrates a strong association among a low CD4/CD8 ratio, a reduced number of germinal centers, and high FOXP3$^+$ cell density with poor patient outcomes (**Fig. 5B**).

In the pPET$^-$ group, univariate analysis identified NETs [$P = 0.0282$; HR (95% CI), 5.576 (1.202–25.875)] and the number of germinal centers [$P = 0.0472$; HR (95% CI), 4.721 (1.020–21.861)] as significantly associated with relapse risk (Supplementary Table S8A). Combination analyses revealed that NETs and germinal centers [$P = 0.0009$; HR (95% CI), 9.537 (2.510–36.235)], as well as NETs and FIGO IIA1 to IIIB [$P = 0.0052$; HR (95% CI), 8.943 (1.923–41.591)], were the most relevant (Supplementary Table S8B). The most predictive model was the combination of NETs, germinal centers, and FIGO IIA1-IIIB, which conferred the highest relapse risk [$P = 0.0003$; HR (95% CI), 12.068 (3.159–46.108); Supplementary Table S8C]. The most relevant single, dual, and triple variable associations for pPET$^-$ patients are illustrated in **Fig. 5D**. Kaplan–Meier plot combining three potent parameters demonstrates a strong association between a high NET density, a reduced number of germinal centers, and FIGO IIA1 to IIIB status with poor patient outcomes (**Fig. 5E**).

The specificity, sensitivity, and accuracy of each signature are presented in **Fig. 5C** and **F**; Supplementary Figs. S7 and S8. The signature related to pPET$^+$ patients demonstrated a perfect positive predictive value (PPV = 1.0) and specificity (1.0), reflecting an excellent capacity to correctly identify patients who relapsed without any false positives. Its sensitivity (0.38) and the NPV were moderate (0.73), indicating that some cases of relapse were not detected (**Fig. 5C**). The second signature for pPET$^-$ patients was more sensitive (0.73) with a lower PPV value (0.53; **Fig. 5F**).

Together, our combinatorial analyses revealed distinct predictive signatures in pPET$^-$ and pPET$^+$ patients with LACC.

Discussion

Despite significant progress in the management of LACC over the past 2 decades, approximately 30% of patients still experience disease recurrence (15). Among known prognostic factors, nodal status plays a central role in treatment planning. In particular, the detection of PAoLN involvement remains critical, as it can lead to disease upstaging and prompt a change in the therapeutic strategy, which can include the use of extended-field radiotherapy (7). We hypothesized that even in the absence of detectable metastatic cells and/or in the case of PET scan negativity at the PAo level, PAoLNs may contain valuable predictive information. A key originality of the present study lies in the in-depth histologic and IHC analysis of whole-scanned sections of PAoLNs, which are typically disregarded once classified as metastasis-free. Our study demonstrates the added value of integrating pPET scan status and PAoLN histologic analyses at diagnosis to predict the risk of relapse.

We conducted a retrospective cohort study of patients with LACC, focusing on those with histopathologically negative PAoLN ($n = 137$). Previous studies have demonstrated an increased risk of PAoLN disease when PET identifies positive pelvic nodes (16, 17).

(*Continued.*) immune cell infiltration expressed as cell density in pPET$^-$ ($n = 46$) and pPET$^+$ ($n = 45$) patient subgroups: CD4/CD8 ratio (**D**), CD4 density (**E**), CD8 density (**F**), FOXP3$^+$ cells (**G**), and CD66b$^+$ cells (**H**). Data are represented by the median with IQRs. Mann–Whitney U tests; *, $P < 0.05$; ns, not significant. **I–P,** Relationship between TA-HEVs and T-cell infiltration in primary tumors. **I,** Representative image showing PNAd$^+$ αSMA$^+$ vessels (TA-HEVs) within the tumor stroma, as identified in **A**. **J,** Tumor samples from 91 patients were separated into four classes based on PNAd$^+$ αSMA$^+$ vessel density in tumor stroma: I (0/mm^2), II (0–1.173/mm^2), III (1.173–4.362/mm^2), and IV (4.362–22.644/mm^2). **K,** Density of TA-HEVs in pPET$^-$ and pPET$^+$ patients. **L,** Distribution (%) of TA-HEV classes in pPET$^-$ and pPET$^+$ subgroups. **M–P.** Spearman correlations between TA-HEVs and immune cell infiltration represented by either TA-HEV classes (histograms, top) or TA-HEV number (scatter plots, bottom): CD8$^+$ cells (**M**), CD4$^+$ cells (**N**), CD66b$^+$ cells (**O**), and FOXP3$^+$ cells (**P**). Correlation coefficients (r_s) and P values are indicated. Data are shown as median with IQRs. Mann–Whitney U or Kruskal–Wallis tests; *, $P < 0.05$; ns, not significant.

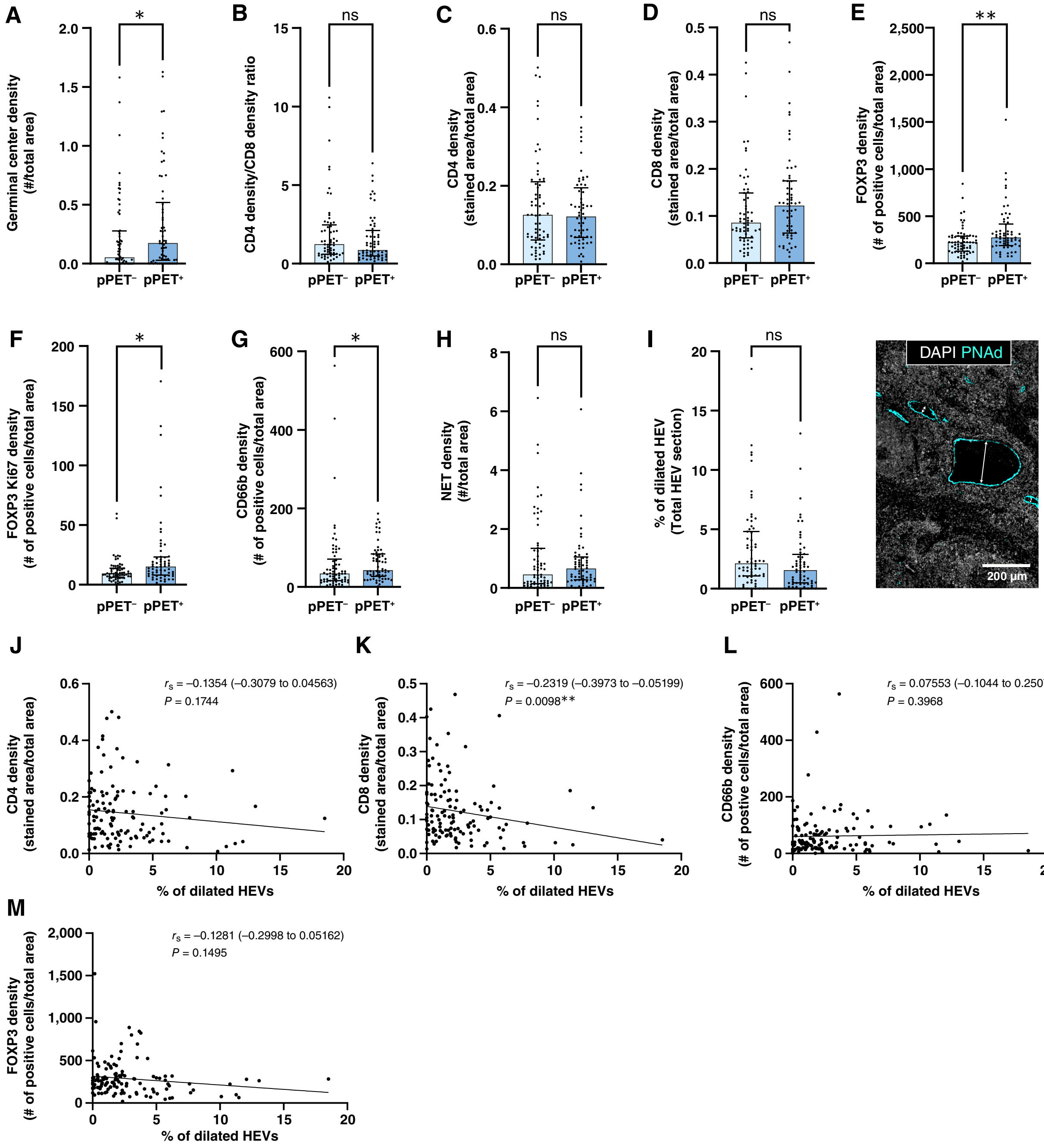

Figure 3.

Impact of pPET scan status on PAoLN remodeling. **A–I,** Densities of immune and vascular parameters assessed by IHC (as described in Figure 3) were compared between pPET$^-$ ($n = 67$) and pPET$^+$ ($n = 62$) patient subgroups: germinal centers (number/mm^2; **A**), CD4/CD8 ratio (**B**), CD4$^+$ cell density (**C**), CD8$^+$ cell density (**D**), FOXP3$^+$ cells/mm^2 (**E**), FOXP3$^+$Ki67$^+$ cells/mm^2 (**F**), CD66b$^+$ cells/mm^2 (**G**), NET density (**H**), and percentage of dilated HEVs (**I**). Dilated HEVs were defined as PNAd$^+$ vessels with a lumen >20 μm, measured as the smallest diameter (as illustrated on the right). **J–M,** Spearman correlations between HEV dilatation and CD4$^+$ (**J**), CD8$^+$ (**K**), CD66b$^+$ (**L**), and FOXP3$^+$ (**M**) cell density. Correlation coefficients (r_s) and P values are indicated. Data are represented as medians with IQRs. Mann–Whitney U tests; *, $P < 0.05$; **, $P < 0.01$; ns, not significant.

Consistently, in our cohort, pelvic LN positivity assessed by imaging was associated with a twofold increase in the risk of relapse. Based on this finding, we conducted a comparative analysis of PAoLN samples from patients with pPET positivity versus pPET negativity. We provide evidence that PAoLNs of patients with pPET positivity displayed enrichment in germinal centers, increased densities of total and proliferating FOXP3$^+$ cells, and a reduced CD4/CD8 ratio. These data suggest a more dynamic and actively regulated immune

Table 1. Risk factors for disease relapse identified by uni- and multivariate analyses.

PAoLN$^-$ pPET$^-$ (*n* = 66)				PAoLN$^-$ pPET$^+$ (*n* = 57)			
Variable	***P* value**	**HR (95% CI)**	**pH test**	**Variable**	***P* value**	**HR (95% CI)**	**pH test**
Non-SCC vs. SCC	0.68	1.313 (0.355–4.850)	0.6398	Non-SCC vs. SCC	0.09	2.336 (0.853–6.395)	0.9979
FIGO IIA1–IIIB vs. IB3	0.54	1.608 (0.352–7.342)	0.6888				
Age	0.26	0.973 (0.927–1.021)	0.4048	Age	0.53	0.986 (0.943–1.031)	0.8669
Tumor size	0.46	1.018 (0.972–1.065)	0.3215	Tumor size	0.53	1.010 (0.978–1.044)	0.1981
Neutrophils/mm^2	0.29	1.313 (0.793–2.173)	0.1777	Neutrophils/mm^2	0.43	1.222 (0.742–2.011)	0.0949
NETs/mm^2†	0.015†	2.768 (1.215–6.304)	0.9733	NETs/mm^2	0.90	1.064 (0.401–2.825)	0.4163
FOXP3$^+$/mm^2	0.78	1.138 (0.459–2.821)	0.1303	FOXP3$^+$/mm^2†	0.040†	1.918 (1.029–3.575)	0.1512
FOXP3$^+$Ki67$^+$/mm^2	0.76	1.119 (0.548–2.286)	0.2341	FOXP3$^+$Ki67$^+$/mm^2†	0.018†	1.668 (1.093–2.544)	0.0586
Germinal center/mm^2	0.089	0.102 (0.007–1.413)	0.2095	Germinal center/mm^2	0.17	0.395 (0.106–1.472)	0.4830
CD4/CD8 ratio†	0.047†	0.497 (0.250–0.989)	0.7125	CD4/CD8 ratio†	0.0097†	0.506 (0.302–0.848)	0.0455†
				CD4/CD8 ratio (corrected)	0.49	0.759 (0.347–1.656)	
				CD4/CD8 ratio × time	0.20	0.967 (0.917–1.019)	
Dilated HEV	0.88	1.048 (0.560–1.959)	0.1466	Dilated HEV	0.60	0.855 (0.474–1.543)	0.2146

PAoLN$^-$ (*n* = 123)

Univariate				Multivariate			Bootstrap (500 resamples)
Variable	***P* value**	**HR (95% CI)**	**pH test**	***P* value**	**HR (95% CI)**	**C-index**	**C-index (95% CI)**
pPET†	0.013†	2.452 (1.204–4.990)	0.16	0.0033†	3.299 (1.488–7.315)	0.7434†	0.7536 (0.666–0.841)
Non-SCC vs. SCC	0.2395	1.613 (0.727–3.576)	0.93	—			
FIGO IIA1–IIIB vs. IB3†	0.044†	1.632 (0.358–7.448)	0.96	—			
FIGO IIIC1–IVA vs. IB3†		3.620 (0.848–15.449)	0.53	—			
FIGO IIA1–IIIB vs. IIIC1–IVA†		0.451 (0.212–0.959)	0.19	—			
Age	0.22	0.980 (0.950–1.012)	0.53	—			
Tumor size	0.058	3.452 (0.961–12.399)	0.028†	—			
Tumor size (corrected)†	0.0088†	17.02 (2.043–141.77)					
Tumor size × time†	0.0572†	1.003 (0.797–1.003)					
Neutrophils/mm^2†	0.096†	1.327 (0.951–1.851)	0.52	—			
NETs/mm^2†	0.071†	1.712 (0.955–3.071)	0.15	—			
FOXP3$^+$/mm^2†	0.015†	1.900 (1.132–3.191)	0.70	—			
FOXP3$^+$Ki67$^+$/mm^2†	0.0032†	1.729 (1.202–2.489)	0.81	—			
Germinal center/mm^2†	0.097†	0.379 (0.120–1.193)	0.57	0.0355†	0.273 (0.081–0.915)		
CD4/CD8 ratio†	0.0004†	0.483 (0.323–0.720)	0.16	0.0010†	0.490 (0.320–0.748)		
Dilated HEV	0.47	0.857 (0.565–1.301)	0.58	—			

Variables that showed an association with relapse risk at a *P* value of <0.1 in univariable analysis were included in the multivariable model (variables included are marked with †).

microenvironment. In parallel, neutrophil density was elevated in these samples of pPET$^+$ patients, as demonstrated by CD66b$^+$ immunodetection. This finding indicates increased innate immune cell infiltration, a phenomenon that remains poorly characterized both in LNs and in LACC (18). Evidence of NET formation, a hallmark of neutrophil activity, showed a positive trend, although it did not reach statistical significance. This apparent discrepancy between neutrophil density and activity might be attributed to technical limitations, as reliable detection of NETs in LN tissue sections remains particularly challenging. To further explore LN remodeling, we investigated HEVs' architecture, specialized vascular structures in secondary lymphoid organs, composed of PNAd-expressing cuboidal endothelial cells (19, 20). PNAd acts as a ligand for L-selectin/CD62L on lymphocytes, thereby mediating their adhesion to HEVs and subsequent entry into the LN. HEV dilation is a recognized alteration of LN architecture, occurring in both inflammatory and tumoral contexts (21). Bekkhus and colleagues (22) reported HEV dilation in tumor-draining LNs of patients with invasive breast carcinoma. However, no major alterations in HEV architecture were observed in our cohort. Interestingly, CD8 density tended to increase in pPET$^+$ patients and showed a negative correlation with HEV dilatation. This suggests that the preservation of structurally intact (less dilated) HEVs in these patients may support efficient CD8$^+$ T-cell recruitment into PAoLN, thereby sustaining local immune activity. In contrast, the enrichment of proliferating FOXP3$^+$ cells in pPET$^+$ patients was not linked to HEV dilation, suggesting that their local expansion is likely driven by *in situ* modulation rather than altered trafficking via HEVs. These findings support the notion that pPET positivity reflects not only tumor burden but also an immunologically primed microenvironment in PAoLN, which may have implications for disease progression and therapeutic responsiveness.

Together, our data reveal alterations in both adaptive (T cells) and innate (neutrophils) immune cell profiles within PAoLNs, even in the absence of detectable metastatic cells. These changes were accompanied by the activation of the humoral immune response,

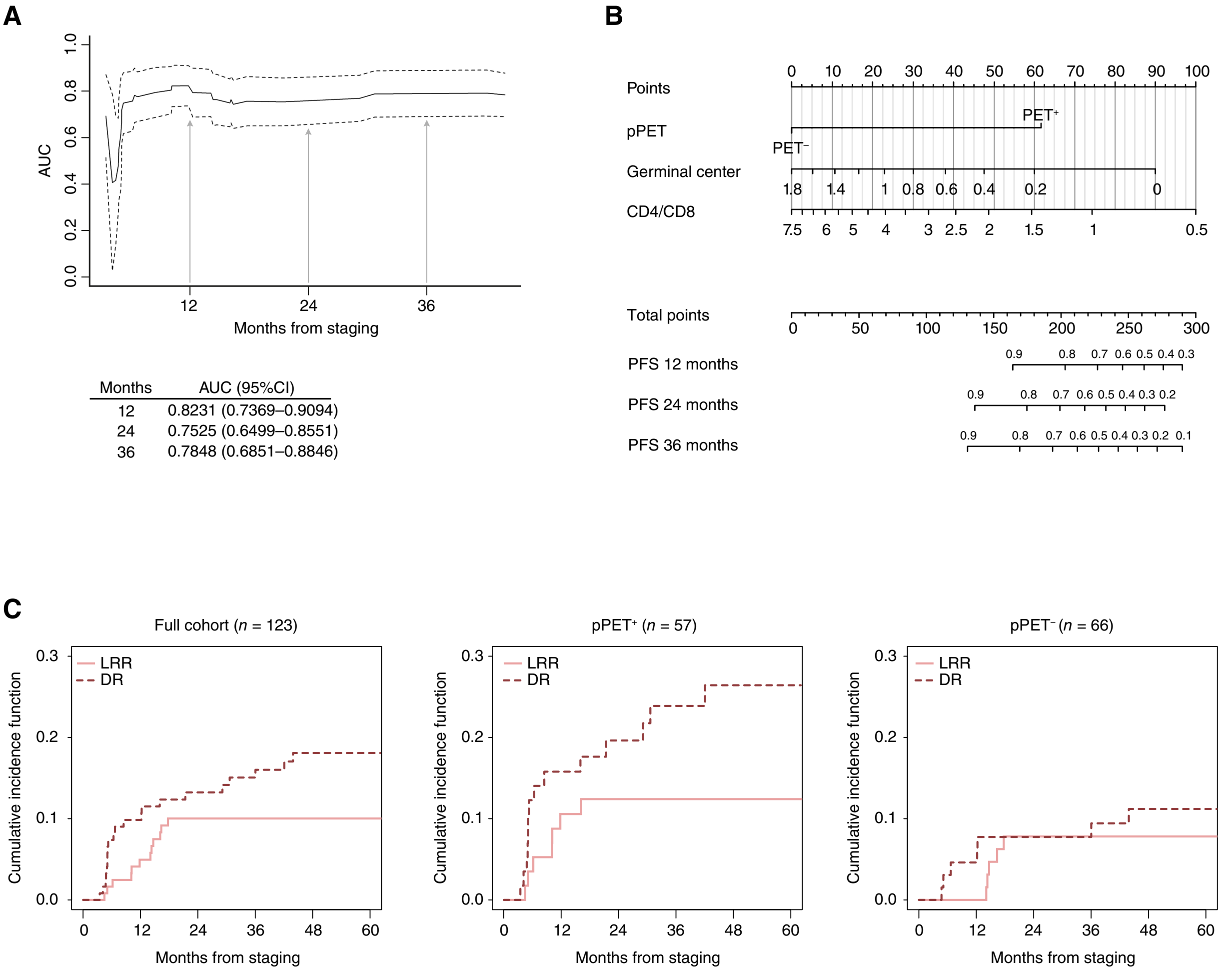

Months	AUC (95%CI)
12	0.8231 (0.7369–0.9094)
24	0.7525 (0.6499–0.8551)
36	0.7848 (0.6851–0.8846)

Figure 4.

Multivariate prognostic model integrating PET status and PAoLN features. **A,** Time-dependent AUC for PFS, with 95% CIs indicated by dashed lines. **B,** Nomogram for PFS prediction. Each covariate is assigned a weighted score proportional to its relative contribution to the model. The total score corresponds to an individualized estimated probability of remaining progression-free at 12, 24, and 36 months. **C,** CIFs for the overall cohort (*n* = 123) and stratified by pPET$^+$ and pPET$^-$ subgroups.

evidenced by an increased number of germinal centers, sites where naive B lymphocytes differentiate into antibody-secreting memory B and plasma cells in response to T cell–dependent antigen. This observation is in line with our previous clinical study, which reported remodeling of B- and T-cell immune landscapes in nonmetastatic pelvic sentinel LNs of patients with early-stage cervical cancer (23). Collectively, these findings point to substantial modifications of LNs, occurring not only within the tumor-draining sentinel LN, as predicted by the “premetastatic niche concept” (24), but also within more distant LNs (25).

In pPET$^+$ patients, we identified a low CD4/CD8 ratio and a high FOXP3$^+$Ki67$^+$ cell density, either independently or in combination, as variables associated with an increased risk of relapse. Notably, the combined evaluation of the CD4/CD8 ratio, FOXP3$^+$ cell density, and number of germinal centers delineated a homogenous subgroup of patients with a 100% risk of disease progression (8/8 patients relapsed, 14% of pPET$^+$ patients). Although the small sample size limits definitive conclusions, this pattern suggests that the immune features of the PAoLN microenvironment may critically affect clinical outcomes. Importantly, the observed modulation of the LN immune microenvironment suggests a cascade-like immune response extending from the pelvic to the PAo regions. These data further support the interest in immunotherapy, particularly in pPET$^+$ patients, which is increasingly considered for LACC treatment regardless of LN status (26–28). This is particularly relevant for cervical cancers, in which persistent HPV infection, detected in more than 90% of cases, is a well-established driver of immune evasion (29). Our study supports the rationale for integrating immunotherapeutic strategies into the management of pPET$^+$ patients although the optimal immune checkpoint targets in this setting remain to be defined.

A key finding of the present study is the discovery of previously unrecognized variables, namely NETs and the number of germinal centers, that can independently, or in combination, predict a high risk of relapse in pPET$^-$ patients. Notably, the combination of NETs, germinal center number and FIGO IIA1 to IIIB stages

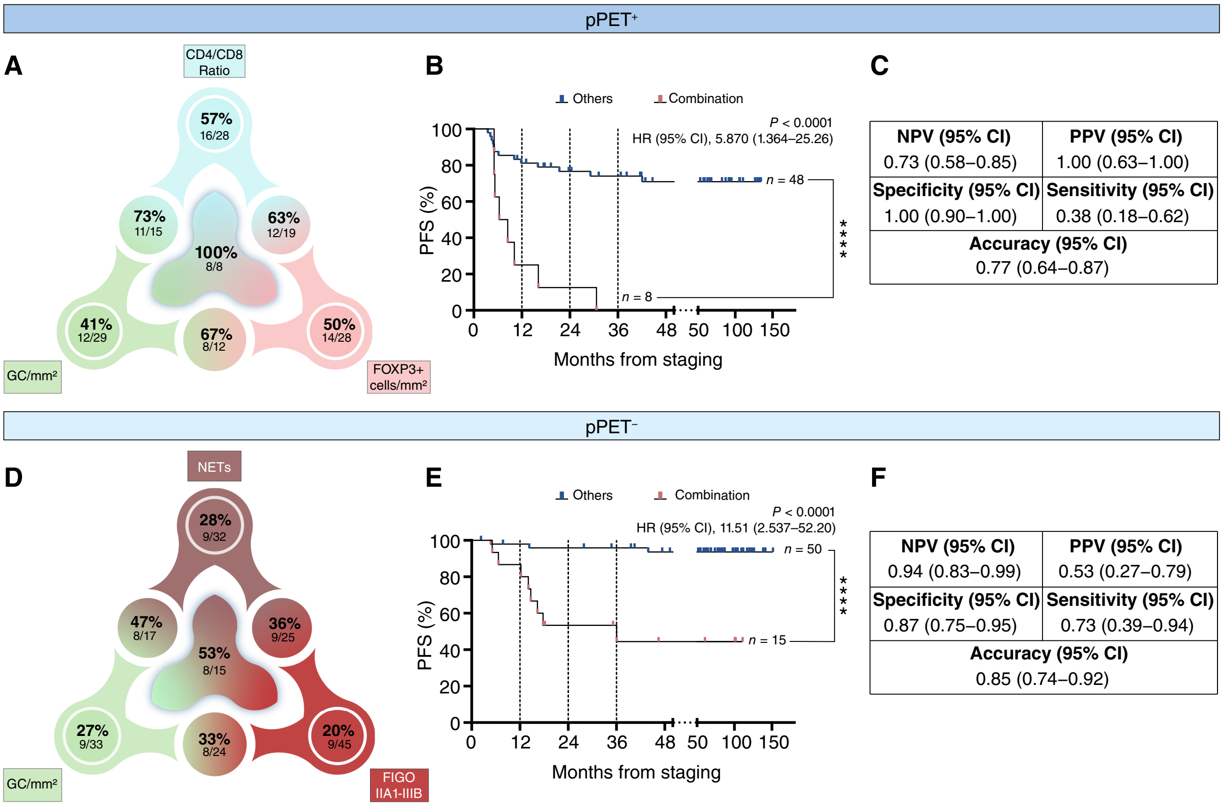

C

NPV (95% CI)	PPV (95% CI)
0.73 (0.58–0.85)	1.00 (0.63–1.00)
Specificity (95% CI)	**Sensitivity (95% CI)**
1.00 (0.90–1.00)	0.38 (0.18–0.62)
Accuracy (95% CI)	
0.77 (0.64–0.87)	

F

NPV (95% CI)	PPV (95% CI)
0.94 (0.83–0.99)	0.53 (0.27–0.79)
Specificity (95% CI)	**Sensitivity (95% CI)**
0.87 (0.75–0.95)	0.73 (0.39–0.94)
Accuracy (95% CI)	
0.85 (0.74–0.92)	

Figure 5.

Predictive combination of factors in pPET$^+$ and pPET$^-$ patients. **A** and **D,** Schematic illustration of the strongest predictive associations of clinical and biological variables. The percentage and number of patients experiencing relapse are indicated. **B** and **E,** Kaplan–Meier curves depicting PFS according to the main predictive combination in pPET$^+$ (**B**) and pPET$^-$ (**E**) patients. **C** and **F,** Diagnostic performance of the main predictive combination in pPET$^+$ (**C**) and pPET$^-$ (**F**) patients with sensitivity, specificity, positive predictive value (PPV), negative predictive value (NPV), and overall accuracy. Log-rank test; ****, $P < 0.0001$.

demonstrated the strongest predictive value. These findings are highly relevant to clinical practice. Indeed, when a PET scan of the pelvic area is negative, the clinical utility of PAoLN staging is currently debated because the risk of PAo nodal involvement is very low, as documented by Uzan and colleagues (16). Of note, previous studies have concluded that in patients with negative pPET status, the risk of PAoLN metastasis is very low (30, 31). The clinical benefit of PAo lymphadenectomy is still debated and is currently being investigated in a phase III randomized clinical trial (PAROLA trial; ref. 32). Although laparoscopic PAo lymphadenectomy is a well-codified technique, particularly in the hands of an experienced surgical team (33), it carries a risk of lymphatic and vascular morbidity and a potential delay in treatment initiation that must be weighed carefully. Our novel findings suggest that PAoLN status after lymphadenectomy remains of interest in patients with negative pelvic LNs on imaging. Given the technical challenges for NET detection, germinal center quantification seems to be a more practical and reproducible approach for routine clinical use. We propose that closer surveillance would be beneficial for these patients. As more than 75% of recurrences occur within the first 2 to 3 years after diagnosis, an intensified follow-up strategy during the high-risk window may be particularly valuable. Ultimately, follow-up schedules should be tailored to individual patients, taking into consideration prognostic factors, treatment modalities, and side effects. In this context, the development of a nomogram derived from the multivariate model represents a clinically meaningful step toward individualized risk stratification. Internal validation was provided using bootstrap resampling with 500 iterations. The temporal stability and robustness of the model are supported by time-dependent AUC values, achieving approximately 0.8 across follow-up. Collectively, these findings highlight the potential clinical utility of this approach to inform risk-adapted surveillance strategies in routine practice. A limitation of this LN study is its single-centered retrospective nature, analyzing only one LN among all resected by laparoscopic lymphadenectomy. Further validation on a prospective cohort would be necessary in future research.

Can we find similar information in the primary tumors and avoid PAo lymphadenectomy associated with postoperative complications (16)? In our cohort, a differential profile of CD8 T-cell infiltration was noted in the tumor stroma of patients according to pPET status. Additionally, the density of TA-HEVs was distinguishable in tumors of pPET$^+$ versus pPET$^-$ patients. However, TA-HEV density was not or very weakly correlated to immune infiltration. Notably, none of the parameters analyzed or combinations tested were predictive of tumor relapse, except for tumor size contributing to FIGO classification and FOXP3$^+$ cell density, in which the prognostic value seems controversial (34–37). These findings limit the possibility of using primary tumor features as reliable indicators for relapse prediction and further support the clinical relevance of examining a combination of practicable and reproducible parameters in PAoLNs.

Together, our study demonstrates the interest of combining clinical and histologic variables to guide therapeutic decision-making, which is in line with the growing trend toward personalized medicine. These observations suggest that treatment strategies may need to be reconsidered or that closer surveillance should be implemented for patients identified as high risk.

Data Availability

Material used to conduct the research and all data supporting the findings of this study are included in this article and its Supplementary Materials. Whole-slide immunohistochemical images are not publicly deposited due to their substantial file size and ethical restrictions associated with patient-derived material. Access to these data may be considered for academic research purposes upon reasonable request to the corresponding author and subject to institutional review and applicable data protection regulations. Quantitative image analyses were performed using the publicly available software QuPath. No custom code or proprietary algorithms were generated for this study. Deidentified clinical summary data may be shared for academic, noncommercial research purposes upon request to the corresponding author and in accordance with Institutional Review Board approval and relevant data protection legislation.

Authors' Disclosures

L. Baudin reports grants from Fonds de la Recherche Scientifique (FNRS) Belgium during the conduct of the study. L. Zanella reports grants from FNRS-Belgium, during the conduct of the study. C. Gennigens reports grants, personal fees, and other support from MSD, Ipsen, and GSK; grants and personal fees from AstraZeneca and EISAI; grants and other support from PharmaMar; and personal fees from Genmab and Deciphera outside the submitted work. S. Pirson reports grants from FNRS-Belgium during the conduct of the study. F. Kridelka reports grants from FNRS-Belgium, Fondation Contre le Cancer, and Fondation Léon Fredericq during the conduct of the study. A. Noel reports grants from FNRS-Belgium, Fondation Contre le Cancer, and Fondation Léon Fredericq during the conduct of the study. No disclosures were reported by the other authors.

Authors' Contributions

L. Baudin: Conceptualization, data curation, formal analysis, validation, investigation, visualization, methodology, writing–original draft, writing–review and editing. **L. Zanella:** Conceptualization, resources, data curation, formal analysis, supervision, funding acquisition, validation, investigation, visualization, methodology, writing–original draft, project administration, writing–review and editing. **A. Lebeau:** Conceptualization, resources, data curation, writing–original draft, writing–review and editing. **C. Pleyers:** Resources, data curation, writing–original draft, writing–review and editing. **N. Gubbels:** Formal analysis, investigation, methodology, writing–original draft, writing–review and editing. **S. Blacher:** Formal analysis, writing–original draft, writing–review and editing. **L. Seidel:** Resources, data curation, formal analysis, writing–original draft, writing–review and editing. **A. Kakkos:** Resources, data curation, writing–original draft, writing–review and editing. **F. Goffin:** Resources, data curation, writing–original draft, writing–review and editing. **P. Lovinfosse:** Resources, data curation, formal analysis, writing–review and editing. **C. Gennigens:** Resources, data curation, writing–original draft, writing–review and editing. **S. Pirson:** Investigation, methodology, writing–original draft, writing–review and editing. **F. Kridelka:** Conceptualization, resources, supervision, funding acquisition, visualization, methodology, writing–original draft, project administration, writing–review and editing. **A. Noel:** Conceptualization, resources, supervision, funding acquisition, visualization, methodology, writing–original draft, project administration, writing–review and editing.

Acknowledgments

The authors thank the Biobank of the University Hospital of Liège (Belgium) for providing human biopsies and Animascience for the elaboration of the graphics. This work was supported by grants from the Fonds de la Recherche Scientifique-FNRS (F.R.S.-FNRS, Belgium), the Fondation contre le Cancer (foundation of public interest, Belgium), the Fonds spéciaux de la Recherche (University of Liège), and the Fondation Hospitalo Universitaire Léon Fredericq (University of Liège). This project has received funding from the Fonds voor Wetenschappelijk Onderzoek – Vlaanderen (FWO) and F.R.S.-FNRS under the Excellence of Science programme (EOS No. 40007532). We thank the Groupe Interdisciplinaire de Génoprotéomique Appliquée (GIGA; University of Liège, Belgium) for access to the various platforms: (i) GIGA-Genomics platform, (ii) GIGA-Proteomics platform, (iii) GIGA-Imaging and Flow Cytometry platform, (iv) GIGA-Bioinformatics platform, and (v) GIGA-Mouse facility and Transgenics platform.

Note

Supplementary data for this article are available at Clinical Cancer Research Online (http://clincancerres.aacrjournals.org/).

Received October 21, 2025; revised January 15, 2026; accepted February 27, 2026; posted first March 4, 2026.

References

1. Bray F, Laversanne M, Sung H, Ferlay J, Siegel RL, Soerjomataram I, et al. Global cancer statistics 2022: GLOBOCAN estimates of incidence and mortality worldwide for 36 cancers in 185 countries. CA Cancer J Clin 2024;74:229–63.
2. Bhatla N, Aoki D, Sharma DN, Sankaranarayanan R. Cancer of the cervix uteri. Int J Gynecol Obstet 2018;143:22–36.
3. Wang W, Liu X, Meng Q, Zhang F, Hu K. Nomograms predicting survival and patterns of failure in patients with cervical cancer treated with concurrent chemoradiotherapy: a special focus on lymph nodes metastases. PLoS One 2019;14:e0214498.
4. Guo T, Zhao Y, Zeng J, Li J, Tang E, Wu L. Examined lymph node counts affected the staging and survival in cervical cancer: a retrospective study using the SEER and Chinese cohort. Ann Med 2025;57:2459821.
5. Guani B, Mahiou K, Crestani A, Cibula D, Buda A, Gaillard T, et al. Clinical impact of low-volume lymph node metastases in early-stage cervical cancer: a comprehensive meta-analysis. Gynecol Oncol 2022;164:446–54.
6. Li J, Liu G, Luo J, Yan S, Ye P, Wang J, et al. Cervical cancer prognosis and related risk factors for patients with cervical cancer: a long-term retrospective cohort study. Sci Rep 2022;12:13994.
7. Cibula D, Raspollini MR, Planchamp F, Centeno C, Chargari C, Felix A, et al. ESGO/ESTRO/ESP Guidelines for the management of patients with cervical cancer – update 2023. Int J Gynecol Cancer 2023;33:649–66.
8. Dheur A, Kakkos A, Danthine D, Delbecque K, Goffin F, Gonne E, et al. Lymph node assessment in cervical cancer: current approaches. Front Oncol 2024;14:1435532.
9. Mathevet P, Lécuru F, Uzan C, Boutitie F, Magaud L, Guyon F, et al. Sentinel lymph node biopsy and morbidity outcomes in early cervical cancer: results of a multicentre randomised trial (SENTICOL-2). Eur J Cancer 2021;148:307–15.
10. Van der Zee AGJ, Oonk MH, De Hullu JA, Ansink AC, Vergote I, Verheijen RH, et al. Sentinel node dissection is safe in the treatment of early-stage vulvar cancer. J Clin Oncol 2008;26:884–9.
11. Institut Claudius Regaud. PARa-aOrtic LymphAdenectomy in locally advanced cervical cancer [internet]. 2025. [cited 2025 Sept 16]. Report No.: NCT05581121. Available from: https://clinicaltrials.gov/study/NCT05581121.
12. Gennigens C, Jerusalem G, Lapaille L, De Cuypere M, Streel S, Kridelka F, et al. Recurrent or primary metastatic cervical cancer: current and future treatments. ESMO Open 2022;7:100579.
13. Pötter R, Tanderup K, Schmid MP, Jürgenliemk-Schulz I, Haie-Meder C, Fokdal LU, et al. MRI-guided adaptive brachytherapy in locally advanced cervical cancer (EMBRACE- I): a multicentre prospective cohort study. Lancet Oncol 2021;22:538–47.
14. Vella G, Hua Y, Bergers G. High endothelial venules in cancer: regulation, function, and therapeutic implication. Cancer Cell 2023;41:527–45.
15. Gennigens C, De Cuypere M, Hermesse J, Kridelka F, Jerusalem G. Optimal treatment in locally advanced cervical cancer. Expert Rev Anticancer Ther 2021;21:657–71.
16. Uzan C, Souadka A, Gouy S, Debaere T, Duclos J, Lumbroso J, et al. Analysis of morbidity and clinical implications of laparoscopic para-aortic lymphadenectomy in a continuous series of 98 patients with advanced-stage cervical

cancer and negative PET-CT imaging in the para-aortic area. Oncologist 2011; 16:1021–7.
17. Acosta Ú, Bebia V, Torné A, Carreras-Dieguez N, Glickman A, Pérez-Benavente A, et al. Topographic mapping of pelvic and aortic lymph node metastases in stage IIIC1r locally advanced cervical cancer: a retrospective study by the Spain-GOG group. Gynecol Oncol 2025;198:49–54.
18. Hampton HR, Chtanova T. The lymph node neutrophil. Semin Immunol 2016;28:129–36.
19. Streeter PR, Rouse BT, Butcher EC. Immunohistologic and functional characterization of a vascular addressin involved in lymphocyte homing into peripheral lymph nodes. J Cell Biol 1988;107:1853–62.
20. Girard JP, Springer TA. High endothelial venules (HEVs): specialized endothelium for lymphocyte migration. Immunol Today 1995;16:449–57.
21. Vella G, Guelfi S, Bergers G. High endothelial venules: a vascular perspective on tertiary lymphoid structures in cancer. Front Immunol 2021;12:736670.
22. Bekkhus T, Martikainen T, Olofsson A, Franzén Boger M, Vasiliu Bacovia D, Wärnberg F, et al. Remodeling of the lymph node high endothelial venules reflects tumor invasiveness in breast cancer and is associated with dysregulation of perivascular stromal cells. Cancers (Basel) 2021;13:211.
23. Balsat C, Blacher S, Herfs M, Van De Velde M, Signolle N, Sauthier P, et al. A specific immune and lymphatic profile characterizes the pre-metastatic state of the sentinel lymph node in patients with early cervical cancer. Oncoimmunology 2017 Feb;6:e1265718.
24. Peinado H, Zhang H, Matei IR, Costa-Silva B, Hoshino A, Rodrigues G, et al. Pre- metastatic niches: organ-specific homes for metastases. Nat Rev Cancer 2017;17:302–17.
25. Gillot L, Lebeau A, Baudin L, Pottier C, Louis T, Durré T, et al. Periostin in lymph node pre-metastatic niches governs lymphatic endothelial cell functions and metastatic colonization. Cell Mol Life Sci 2022;79:295.
26. Tewari KS. Cervical cancer. N Engl J Med 2025;392 :56–71.
27. Ogasawara A, Hasegawa K. Recent advances in immunotherapy for cervical cancer. Int J Clin Oncol 2025;30:434–48.
28. Lorusso D, Xiang Y, Hasegawa K, Scambia G, Leiva M, Ramos-Elias P, et al. Pembrolizumab or placebo with chemoradiotherapy followed by pembrolizumab or placebo for newly diagnosed, high-risk, locally advanced cervical cancer (ENGOT- cx11/GOG-3047/KEYNOTE-A18): overall survival results from a randomised, double- blind, placebo-controlled, phase 3 trial. Lancet 2024;404: 1321–32.
29. Ling J, Sun Q, Tian Q, Shi H, Yang H, Ren J. Human papillomavirus 16 E6/E7 contributes to immune escape and progression of cervical cancer by regulating miR-142– 5p/PD-L1 axis. Arch Biochem Biophys 2022;731:109449.
30. Martinez A, Voglimacci M, Lusque A, Ducassou A, Gladieff L, Dupuis N, et al. Tumour and pelvic lymph node metabolic activity on FDG-PET/CT to stratify patients for para- aortic surgical staging in locally advanced cervical cancer. Eur J Nucl Med Mol Imaging 2020;47:1252–60.
31. De Cuypere M, Lovinfosse P, Goffin F, Gennigens C, Rovira R, Duch J, et al. Added value of para-aortic surgical staging compared to 18F-FDG PET/CT on the external beam radiation field for patients with locally advanced cervical cancer: an ONCO-GF study. Eur J Surg Oncol 2020;46:883–7.
32. Martinez A, Lecuru F, Bizzarri N, Chargari C, Ducassou A, Fagotti A, et al. PARa-aOrtic LymphAdenectomy in locally advanced cervical cancer (PAROLA trial): a GINECO, ENGOT, and GCIG study. Int J Gynecol Cancer 2023;33:293–8.
33. Lin Z, Liu Z, Chen J, Gu H, Liu G, Liu J, et al. Novel anatomical concept and standardized technique for single-port Paraaortic lymphadenectomy in gynecological cancers. Gynecol Oncol 2025;201:176–83.
34. deLeeuw RJ, Kost SE, Kakal JA, Nelson BH. The prognostic value of FoxP3+ tumor- infiltrating lymphocytes in cancer: a critical review of the literature. Clin Cancer Res 2012;18:3022–9.
35. Punt S, van Vliet ME, Spaans VM, de Kroon CD, Fleuren GJ, Gorter A, et al. FoxP3(+) and IL-17(+) cells are correlated with improved prognosis in cervical adenocarcinoma. Cancer Immunol Immunother 2015;64:745–53.
36. Li L, Xu XT, Wang LL, Qin SB, Zhou JY. Expression and clinicopathological significance of Foxp3 and VISTA in cervical cancer. Am J Transl Res 2021;139: 10428–38.
37. Shang B, Liu Y, Jiang Sjuan, Liu Y. Prognostic value of tumor-infiltrating FoxP3+ regulatory T cells in cancers: a systematic review and meta-analysis. Sci Rep 2015;5:15179.